

Università degli studi di Padova

Introduction to research

Report On

Characterization of a detector for ionizing radiation and data analysis in the context of the ISOLPHARM project

Student: Federico Simioni

Tutor: Prof. Lunardon Marcello

Co-tutor: Dott. Serafini Davide

Abstract

The student will study the functioning of a specific ionizing radiation detector and its possible use in a context of medical physics. She/he will learn to setup the detector, run the data acquisition and understand the acquired energy spectra. She/he will then use the GEANT4 software with the aim of describing the response of the detector and estimating the efficiency. Finally, real data related to the activity biodistribution of a chelated radionuclide in mice obtained in an experiment for the ISOLPHARM project will be analyzed.

Contents

1	Introduction	4
1.1	ISOLPHARM project	4
1.2	Experimental apparatus	5
1.3	GEANT4	6
2	Detector characterization and modellization	6
2.1	Experimental setup	6
2.2	Energy calibration and FWHM	7
2.3	Photopeak efficiency	9
2.4	Simulations	9
2.5	Test of the acquisition rate	11
3	Data analysis	12
4	Conclusions	15
5	Appendix	16
5.1	Photopeak efficiency	16
5.2	Simulations	16
5.3	Data analysis	16

List of Figures

1	Radiopharmaceutical schematic representation [2]	4
2	Scheme of the entire process, from production to injection of the radiopharmacautical [2]	5
3	Experimental apparatus	6
4	Graphical representation of experimental setup	7
5	Experimental setups	7
6	Fit of FWHM with respect to E	8
7	Absolute photopeak efficiency with respect to the distance between sources and detector	9
8	Differences between spectra of ^{22}Na obtained with and without smearing	10
9	Overlap between spectrum obtained by simulation (red one) and measurement (blue one) with ^{137}Cs at P1	10
10	Simulated absolute photopeak efficiencies with respect to the distance from detector	11
11	Experimental setup with new source-holder	12
12	Average %ID/g for CCK2R mice	14
13	Average %ID/g for WT mice	14
14	%ID/g for CCK2R mice, PET at 30 minutes	19
15	%ID/g for CCK2R mice, PET at 2 hours	19
16	%ID/g for WT mice, PET at 30 minutes	20
17	%ID/g for WT mice, PET at 2 hours	20

1 Introduction

1.1 ISOLPHARM project

Radiopharmaceuticals are drugs containing radionuclides and are commonly used in nuclear medicine for the diagnosis or treatment of various diseases, primarily tumors [1]. Their structure is shown Figure 1 and, as we can see, it is composed of various components [2]:

- **RADIOISOTOPE:** addressed later
- **CHELATOR:** a molecule designed to keep the radionuclide bound to the rest of the molecule
- **LINKER:** connects the chelator to the targeting agent
- **TARGETING AGENT:** typically composed of a small molecule, protein, or antibody that allows the radiopharmaceutical to bind to the cancerous target.

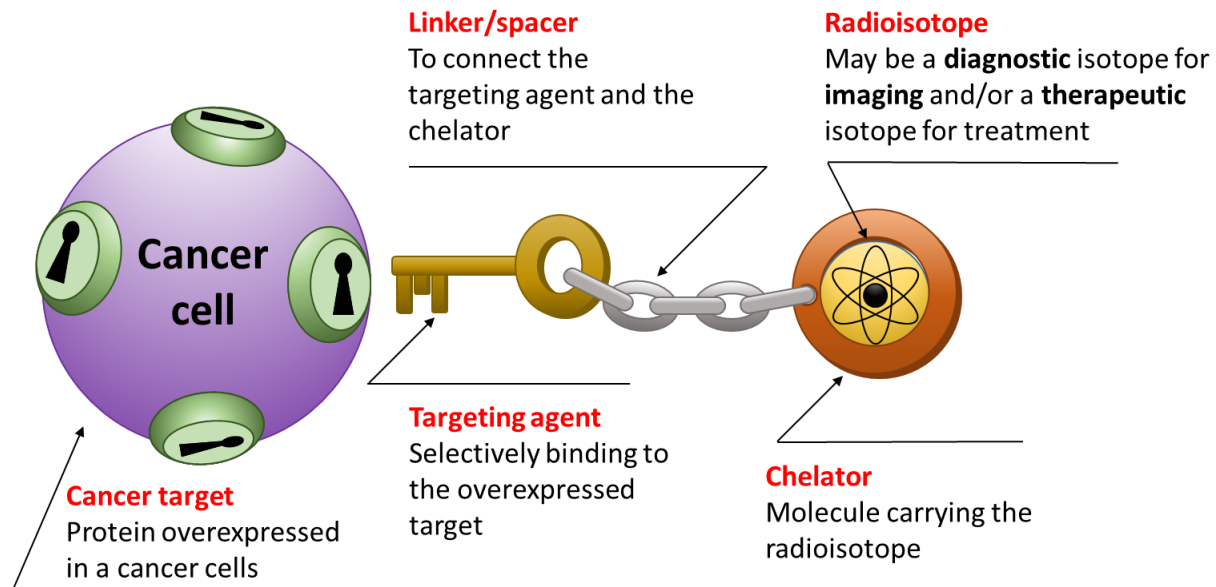


Figure 1: Radiopharmaceutical schematic representation [2]

The underlying principle of these studies is that the cancer cell produces an abundance of proteins, which can be used as targets for radiopharmaceuticals. Clearly, this is one of the fundamental aspects, and developing a suitable technique for their precise localization at disease sites is one of the major challenges to ensure that nuclear medicine plays a more prominent role in clinical practice. Another point receiving significant attention is the availability of isotopes for both diagnostic and therapeutic purposes [3]. In this regard, in terms of therapeutic purposes, α and β^- radiations are commonly used, which allow for the destruction of the cell. For diagnostic purposes, the utilized radiations are typically γ and β^+ (which later annihilates, producing two gamma rays). The production of radionuclides used in radiopharmaceuticals is typically carried out using cyclotrons or nuclear reactors. However, both of these methods come with significant challenges. To address these and explore new ways for obtaining high-purity radionuclides, researchers are actively considering alternative production techniques. One such approach is the use of the ISOL (Isotope Separation On-Line) method, which is the primary technique in the field of

nuclear physics for generating Radioactive Ion Beams. The SPES-ISOLPHARM project, based at INFN-LNL (Istituto Nazionale di Fisica Nucleare-Laboratori Nazionali di Legnaro), is leading a feasibility study focused on the production of isotopes tailored for medical applications. This study exploits SPES (Selective Production of Exotic Species), which is the upcoming ISOL facility currently under construction at LNL. This innovative technique enables the production of both traditional and novel radionuclides with exceptionally high specific activity, pushing the boundaries of radiopharmaceutical research beyond its current state [3]. In addition to production, as can be seen from Figure 2, there are other steps that include [5]:

- Collecting the produced and selected isotopes through targets composed of compressed various possible materials (NaCl , NaNO_3 , and Cellulose-based, ...);
- Chemical separation to selectively isolate the nuclide of interest;
- Radiopharmaceutical assembly (see Figure 1);
- Testing the resulting radioisotope drug through in-vitro and in-vivo experiments.

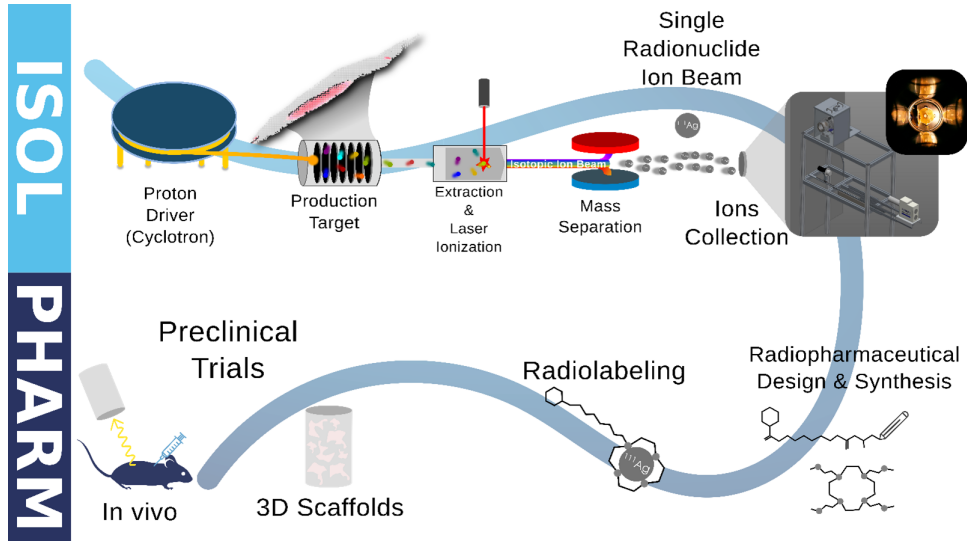
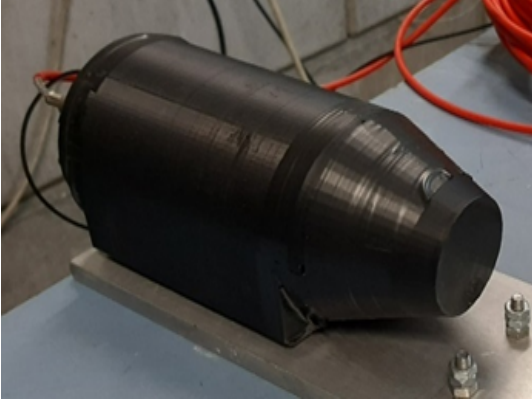


Figure 2: Scheme of the entire process, from production to injection of the radiopharmacautical [2]

1.2 Experimental apparatus

The instrumental apparatus used is depicted in Figure 3. This has been designed with the aim of addressing the need for a relatively cost-effective tool capable of measuring the biodistribution of radiopharmaceuticals in vivo (gamma counter), while maintaining ease of transport between different laboratories and sufficient energy resolution to distinguish closely spaced energy transitions [4]. Regarding the detector, it consists of an inorganic scintillator crystal made of Lanthanum Bromo-Chloride (LBC, $\text{LaBr}_{2.85}\text{Cl}_{0.15} : \text{Ce}$), which is cylindrical in shape with dimensions of 1" x 1". This crystal is manufactured by SCIONIX and is encapsulated in an aluminum casing for hygroscopic reasons. The crystal is optically coupled through a hermetically sealed Quartz window with a Hamamatsu R11102 PhotoMultiplier Tube (PMT) that features a Bialkali photocathode. The PMT is operated at a voltage of -575V.



(a) Detector (with PMT)



(b) Power supply



(c) Digitizer

Figure 3: Experimental apparatus

As for the high-voltage supply for the PMT, it is provided by a CAEN-DT5471N USB HV Power Supply. The anode signal from the PMT is digitized using a CAEN-DT5725 desktop digitizer module, which is an 8-channel, 14-bit, 250MS/s device. The control software used for this setup is an open-source distributed data acquisition system called ABCD¹.

1.3 Geant4

To estimate various quantities related to the detector (such as the photopeak efficiency), a very useful approach involves conducting simulations using GEANT4.

GEANT4 is an open-source C++ Toolkit developed by CERN for simulating the passage of particles and radiation through matter using Monte Carlo methods. It allows us to simulate any setup, detector, or radiation source by selecting which physical quantities (related to primary or secondary interactions between radiation and matter) to output. As it is a toolkit, using it requires developing our own application using custom-defined classes derived from GEANT4 primitives [4]. All the classes, from the mandatory ones (Detector Construction, PhysicsList, and Primary Generator Action Classes) to those essential for characterizing our simulation and extracting the desired information (run-level, event-level, step-level, Sensitive Detector, and Hit Classes), have been derived from the doctoral thesis of Dr. Luca Morselli. In the following image (Figure 4), a graphical representation of the experimental setup described in the next paragraph is presented, created using GEANT4.

2 Detector characterization and modellization

2.1 Experimental setup

Throughout the data collection process, the experimental apparatus mentioned earlier was arranged in the following manner (Figure 5). As can be seen from the photos, an aluminum guide was employed to provide fixed points for securing both the detector and the radioactive samples for analysis. This ensured that there was no risk of accidentally displacing anything, thereby compromising the system's geometry and maintaining uniformity. The different positions were denoted

¹<https://gitlab.com/cristiano.fontana/abcd>

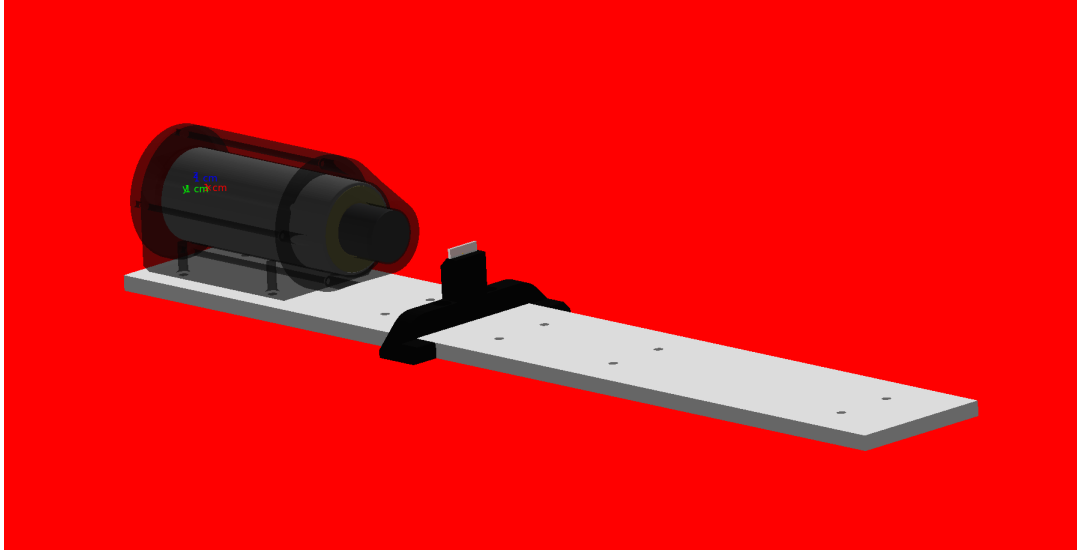


Figure 4: Graphical representation of experimental setup



(a) Top view



(b) Detector and source holder

Figure 5: Experimental setups

in increasing order (from nearest to farthest from the detector) as P1 (1 cm), P2 (6 cm), P3 (11 cm), P4 (21 cm), and P5 (41 cm). The same notation has been consistently used throughout this report.

The sealed radioactive sources used are those listed in Table 1 (with their respective estimated current activities).

2.2 Energy calibration and FWHM

To characterize the detector in question, we began by calibrating it in terms of energy. Regarding the fitting of the characteristic peaks, we opted for a quadratic function ($f(x) = p_0 + p_1 \cdot x + p_2 \cdot x^2$), and the obtained parameters are reported in Table 2, along with the corresponding graph.

Once this was done, taking into account the same spectra used for calibration, we generated a graph depicting the Full Width at Half Maximum (FWHM) as a function of the corresponding peak energy. For the fitting of these data, we employed the following function:

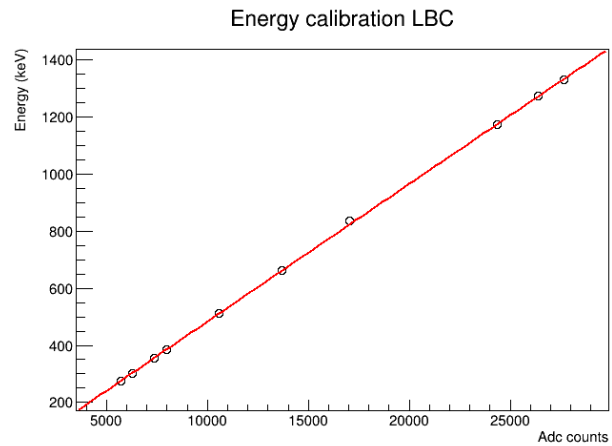
$$\text{FWHM}(E) = a_0 + a_1 \cdot \sqrt{E} + a_2 \cdot E \quad (1)$$

Source	T(1/2)	Initial Activity (kBq)	Actual activity (kBq)
^{241}Am	432.6y	392	387 ± 11
^{133}Ba	10.551y	405	235 ± 7
^{137}Cs	30.08y	386	319 ± 10
^{57}Co	271.74d	377	0.167 ± 0.005
^{60}Co	1925.28d	383	129 ± 4
^{203}Hg	46.594d	985	$(2.76 \pm 0.08) \cdot 10^{-17}$
^{54}Mn	312.2d	422	0.51 ± 0.02
^{22}Na	2.6018y	384	42 ± 1
^{88}Y	106.626d	408	$(65 \pm 1) \cdot 10^{-5}$

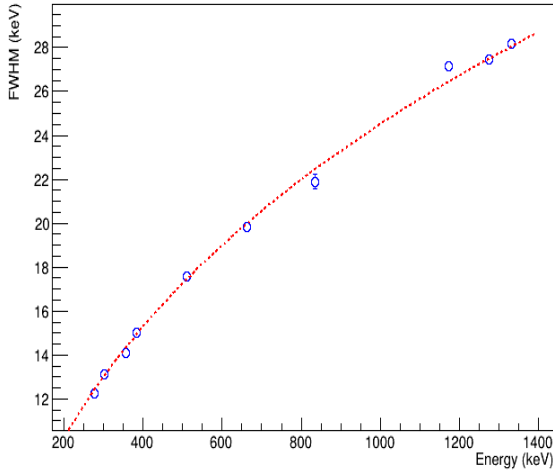
Table 1: Sources available

Parameter	Value
p0 [keV]	-1.50 ± 0.04
p1 [keV/ch]	$(48688 \pm 6) \cdot 10^{-6}$
p2 [keV/ch ²]	$(-1.58 \pm 0.02) \cdot 10^{-8}$

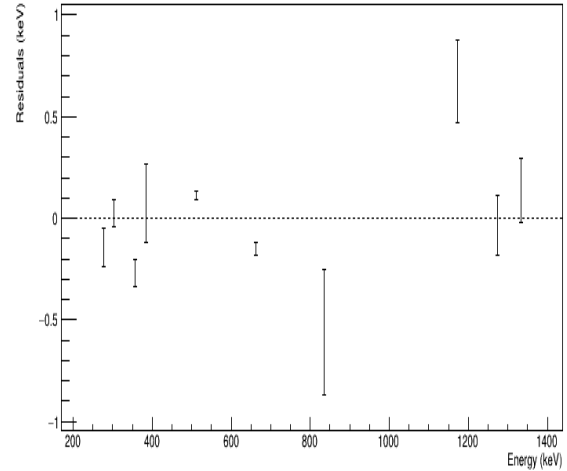
Table 2: Fitting parameters of calibration curve



The obtained results are presented in Figure 6 and Table 3.



(a) Fitting curve of FWHM(E)



(b) Residuals

Figure 6: Fit of FWHM with respect to E

Parameter	Value
a_0 [keV]	-3.2 ± 0.4
a_1 [keV $^{1/2}$]	1.01 ± 0.03
a_2	-0.0042 ± 0.0006

Table 3: Fitting parameters of FWHM(E)

2.3 Photopeak efficiency

To investigate the absolute efficiency of the photopeak and simultaneously compare it with GEANT4 simulations, some of the previously mentioned sources were employed. In addition to exploiting the opportunity to access gamma rays at various energies, these sources were positioned at increasing distances using the aluminum support on which the detector and sources were placed. The efficiency values as a function of the distances from the detector for different energies are presented in a single graph (Figure 7), while the corresponding values are tabulated in the Appendix.

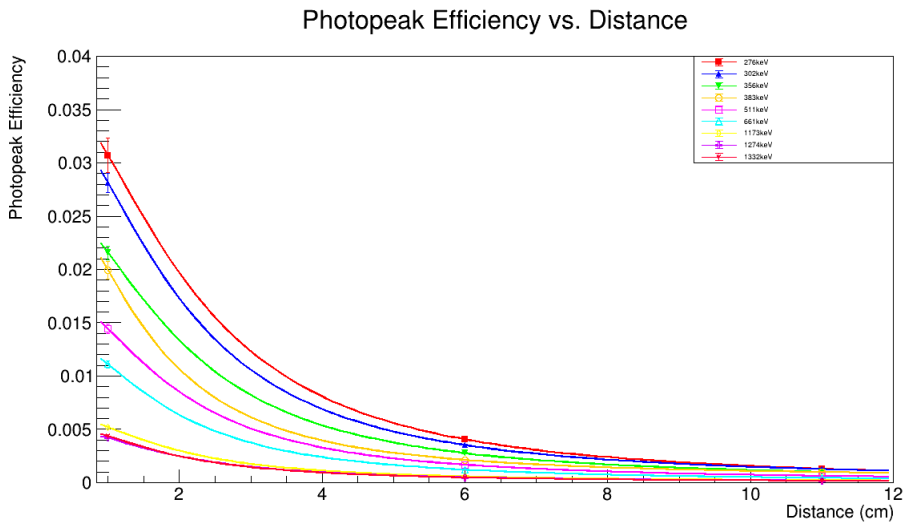


Figure 7: Absolute photopeak efficiency with respect to the distance between sources and detector

2.4 Simulations

Based on the previously obtained FWHM trend, it is feasible to incorporate it into a ROOT macro to generate spectra consistent with those obtained experimentally, using the results provided by the simulations. These simulations, in fact, do not take into account the various stochastic processes that occur from the production of light in the radiation-matter interaction to its collection (not to mention everything that follows in the crystal to amplify the signal, which in turn degrades the resolution). Therefore, what is done is to associate a Gaussian probability distribution with each event.

$$E \rightarrow N(E, \sigma(E))$$

Here, the sigma is obtained precisely from the FWHM fit. As an illustrative example, we present graphs (Figure 8), both with and without this adjustment.

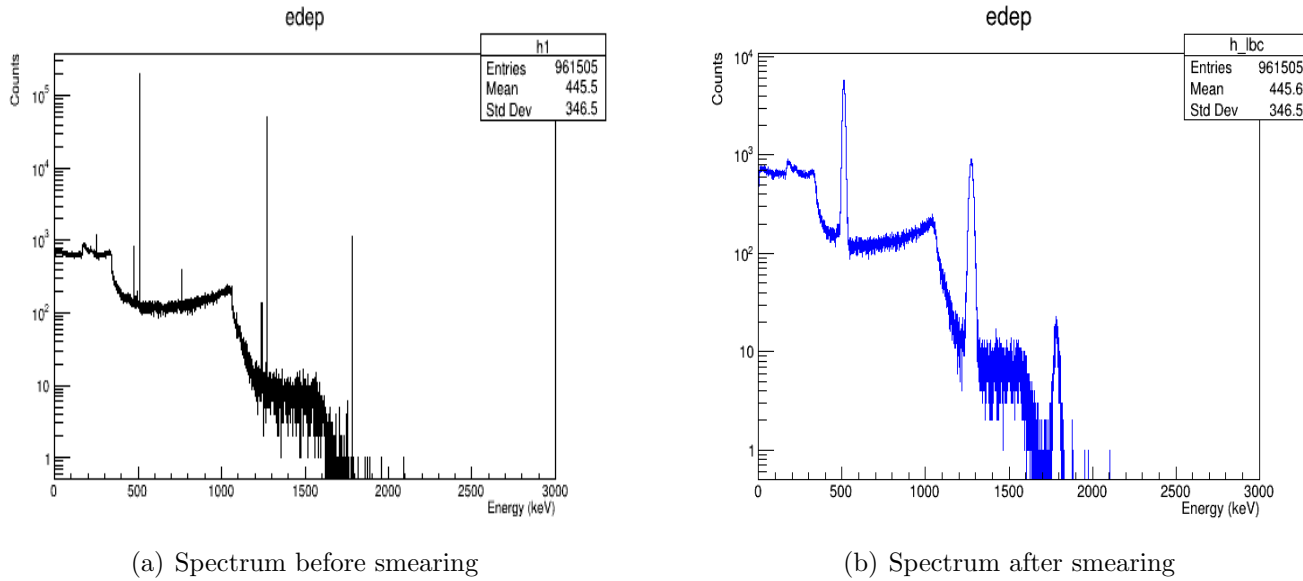


Figure 8: Differences between spectra of ^{22}Na obtained with and without smearing

To demonstrate the consistency between the spectra obtained through simulations and those obtained through actual measurements, the overlap of the two is presented for ^{137}Cs at P1 in Figure 9.

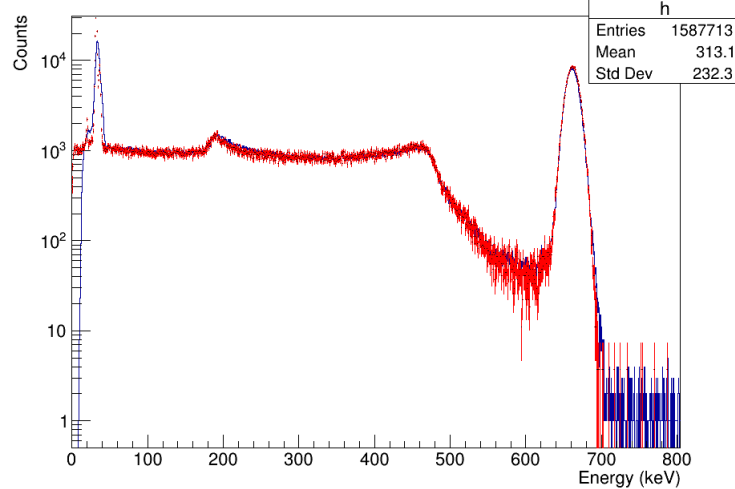


Figure 9: Overlap between spectrum obtained by simulation (red one) and measurement (blue one) with ^{137}Cs at P1

By simulating each source at various positions, it was possible to determine the absolute photopeak efficiency for each of them. The results obtained are presented in Figure 10 (while the various values are reported in the Appendix in tabular form).

The obtained values are found to be consistent with the experimental ones, and as an example, compatibility indices for three different energies are presented in Table 4.

Given the compatibilities, simulations were employed in the subsequent analysis to derive characteristic parameters such as the photopeak efficiencies, which, as we will see, are necessary for

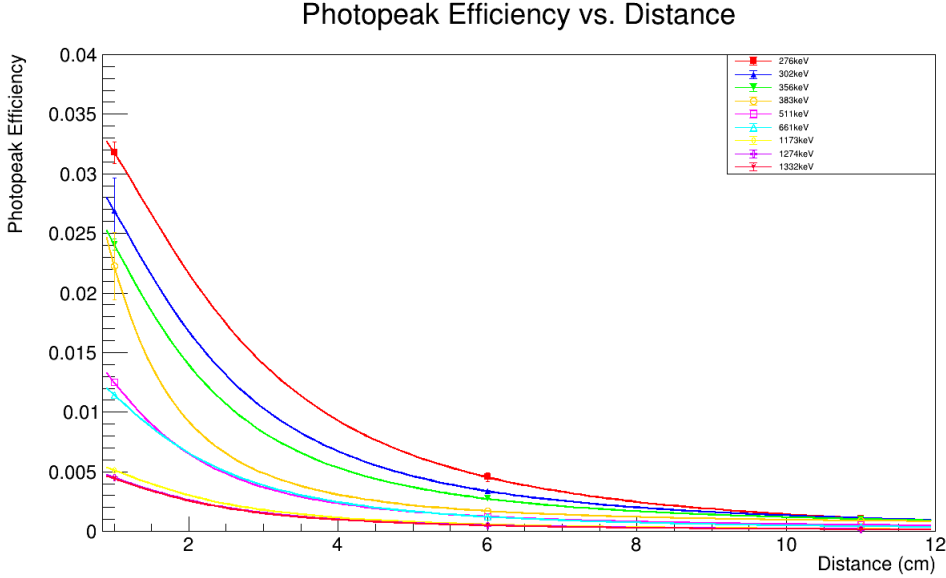


Figure 10: Simulated absolute photopeak efficiencies with respect to the distance from detector

Energy (keV)	P1	P2	P3
276	0.6	1.8	0.8
611	1.0	0.2	1.5
1332	0.3	0.7	0.9

Table 4: Compatibilities between simulations and experimental efficiencies

biodistribution estimations.

2.5 Test of the acquisition rate

The various measurements performed to determine the absolute efficiency of the photopeak, mentioned earlier, were carried out to investigate the behavior of the detector and its acquisition rate (due to some inconsistencies observed in previous measurements prior to this experiment). The reason for using different positions was to manipulate the geometric efficiency in order to vary the incident radiation rate on the detector. Following the successful performance (in line with simulations), it was decided to proceed with further measurements using multiple sources simultaneously. To accomplish this, a new source holder was employed, as shown in Figure 11. In this case, the source holder did not have the necessary holes to fix the position beforehand. Therefore, to achieve a stable position, slight adjustments were made to the distances, without, however, affecting our objectives or goals. Specifically, screws were employed, fastened into various positions on the guide (P1, P2, P3, ...) as references, starting with those corresponding to position P1 (i.e., the closest one).

To avoid complicating the analysis of the obtained spectra, and considering that the range to be tested did not exceed samples with activities greater than 1 MBq, it was decided to use ^{133}Ba , ^{137}Cs , and ^{241}Am as sources (the latter added after testing the first two together). These isotopes, indeed, exhibit spectra with peaks that do not interfere with each other. Regarding the ^{133}Ba peaks, they belong to a flat region of the ^{137}Cs spectrum (while ^{241}Am was only used to increase the total activity, so its peaks were not considered). As can be seen from the table provided



Figure 11: Experimental setup with new source-holder

here, no significant differences were observed, confirming the proper functioning of the detector's acquisition.

276keV	302keV	356keV	383keV	661keV
0.0097 ± 0.0005	0.0091 ± 0.0003	0.0080 ± 0.0003	0.0070 ± 0.0004	0.0047 ± 0.0001

Table 5: Absolute photopeak efficiencies for single sources

276keV	302keV	356keV	383keV	661keV
0.011 ± 0.001	0.0081 ± 0.0003	0.0077 ± 0.0002	0.0074 ± 0.0004	0.0047 ± 0.0001

Table 6: Absolute photopeak efficiencies for case $^{133}\text{Ba} + ^{137}\text{Cs}$

276keV	302keV	356keV	383keV	661keV
0.012 ± 0.002	0.0092 ± 0.0007	0.0084 ± 0.0004	0.0088 ± 0.0004	0.0047 ± 0.0001

Table 7: Absolute photopeak efficiencies for case $^{133}\text{Ba} + ^{137}\text{Cs} + ^{241}\text{Am}$

As can be observed, these tables contain only one position, namely the closest one. The decision not to consider other positions was made because this position already corresponds to the highest incident rate values towards the detector. Therefore, ensuring proper functionality at this position automatically implies the same for the others.

3 Data analysis

Once the detector has been characterized and modeled, it becomes possible to use it for in-vitro and in-vivo experiments, exploiting its capability to count incident gamma rays.

The analysis focused on measurements taken on 4 distinct days, involving nude BALB/c mice carrying A549 xenografted tumors. These mice were divided into 2 categories:

- CCK2R: mice in which the tumor developed the cholecystokinin receptor 2 (CCK2R), used as a target and extensively studied due to its abundance in various types of tumors.
- WILD TYPE: mice in which the tumor did not express the aforementioned receptor.

For each of these mice, the procedure was the same and consisted of the injection of the radiopharmaceutical containing the radionuclide ^{68}Ga (emitting gamma rays at 511 keV), followed by a PET scan after a time interval of 30 minutes or 2 hours. Subsequently, they were sacrificed, and the activity in each organ was measured to estimate the biodistribution.

From the obtained spectra, it was possible to determine the number of counts under the photopeak, from which the specific activity was calculated, taking into account the timing of the injection, the start of data acquisition, and the end (along with their respective time intervals).

Considering, indeed, the well-known decay law: $N(t) = N(0) * e^{-\frac{t}{\tau}} = N(0) * 2^{-\frac{t}{T_{1/2}}}$ (where t represents the time elapsed from the initial moment, τ is the average lifetime of the radionuclide, and $T_{1/2}$ is its half-life), it is possible to derive the quantity ΔN corresponding to the integral of the previously mentioned photopeak.

In fact:

$$\begin{aligned}
 \Delta N &= (N(t_0) - N(t_1)) \cdot \epsilon \cdot Br \\
 &= (N(0) \cdot 2^{-\frac{t_0}{T_{1/2}}} - N(0) \cdot 2^{-\frac{t_1}{T_{1/2}}}) \cdot \epsilon \cdot Br \\
 &= N(0) \cdot 2^{-\frac{t_0}{T_{1/2}}} \cdot [1 - 2^{-\frac{t_1-t_0}{T_{1/2}}}] \cdot \epsilon \cdot Br \\
 &= \frac{N(0)}{T_{1/2}} \cdot \ln(2) \cdot \frac{T_{1/2}}{\ln(2)} \cdot 2^{-\frac{t_0}{T_{1/2}}} \cdot [1 - 2^{-\frac{t_1-t_0}{T_{1/2}}}] \cdot \epsilon \cdot Br \\
 &= A(0) \cdot 2^{-\frac{t_0}{T_{1/2}}} \cdot \frac{T_{1/2}}{\ln(2)} \cdot [1 - 2^{-\frac{t_1-t_0}{T_{1/2}}}] \cdot \epsilon \cdot Br
 \end{aligned}$$

Where ϵ refers to the absolute efficiency of the photopeak and Br to the branching ratio of the γ at the energy considered for the radionuclide under study. From this relation, it is possible to derive an expression for $A(0)$, which can be seen as a sort of "Equivalent initial activity". This is convenient because, dividing this by the total activity of the radiopharmaceutical injected and the weight of the organ under study, we are able to estimate the value of the parameter %ID/g, an indicator used to quantify the fraction of the initial dose injected (per unit of weight) into the considered organ (ID stands for injected dose).

In the Appendix, the various quantities just mentioned are reported, divided by days and types of mice, considering the different organs for each of them.

In Figure 12 and 13, you can see the final results obtained, considering the time intervals between administration and PET and the type of mouse considered.

As can be observed, for the targeted mice, two hours after administration, a significant fraction of the radiopharmaceutical is present in the tumor, unlike the WT ones in which similar behaviors cannot be observed. This result demonstrates the effectiveness of utilizing CCK2R receptors to guide the radiopharmaceutical to the site of interest, although further studies are still needed to confirm its efficacy.

Average CCK2R

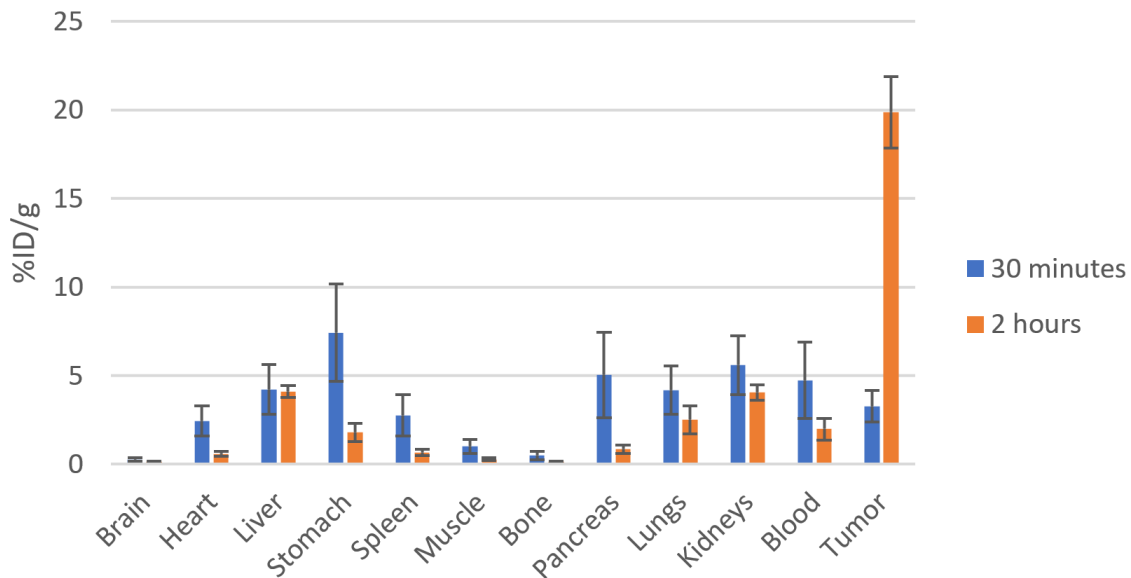


Figure 12: Average %ID/g for CCK2R mice

Average WT

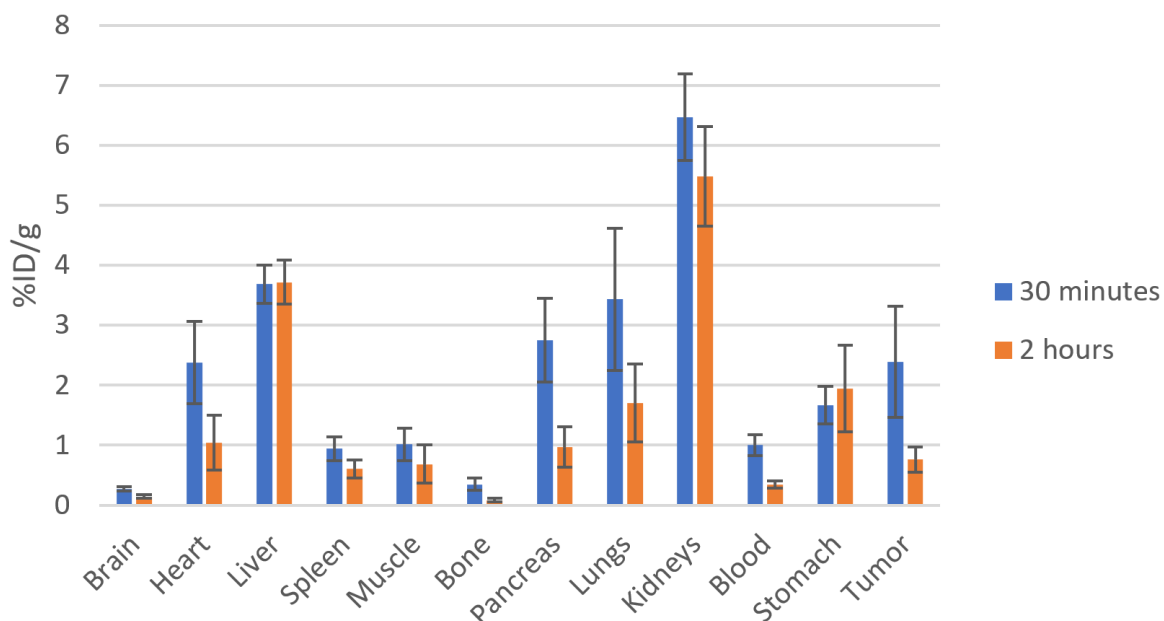


Figure 13: Average %ID/g for WT mice

4 Conclusions

In conclusion, the work conducted during this internship can be summarized as follows:

- A detector (consisting of an inorganic LBC scintillator) was characterized, with energy calibration and an assessment of FWHM behavior as a function of energy.
- Building upon this, a comparison was made between experimentally obtained spectra and those generated through simulations, revealing coherence between the two.
- The acquisition rate of the detector was tested, and no malfunctions were observed.
- An analysis was performed on data collected in previous months, focusing on the biodistribution studies of radiopharmaceuticals, and determining the trend of the injected dose fraction for each organ (%ID/g).

Regarding the latter aspect, the trend exhibits promising results; however, further studies are required to validate these findings.

5 Appendix

5.1 Photopeak efficiency

In Table 8 are reported the absolute photopeak efficiencies derived from measurements.

$\epsilon(\cdot 10^{-3})$	@P1	@P2	@P3	@P4	@P5
276keV	31 ± 2	4.1 ± 0.2	1.3 ± 0.1	/	/
302keV	28.1 ± 0.9	3.5 ± 0.1	1.26 ± 0.04	/	/
356keV	21.5 ± 0.7	2.77 ± 0.09	1.00 ± 0.03	/	/
383keV	19.9 ± 0.8	2.13 ± 0.08	0.98 ± 0.04	/	/
511keV	14.4 ± 0.4	1.68 ± 0.05	0.62 ± 0.02	0.189 ± 0.006	0.053 ± 0.002
661keV	11.1 ± 0.3	1.21 ± 0.04	0.43 ± 0.01	0.131 ± 0.005	0.038 ± 0.001
1173keV	5.2 ± 0.2	0.58 ± 0.02	0.213 ± 0.007	/	/
1274keV	4.2 ± 0.1	0.49 ± 0.02	0.175 ± 0.007	0.057 ± 0.002	0.0158 ± 0.0006
1332keV	4.4 ± 0.1	0.47 ± 0.02	0.170 ± 0.006	/	/

Table 8: Experimental absolute photopeak efficiency. The various position (P1, P2, P3,...) refers to those described in paragraph 2.1

5.2 Simulations

In Table 9 are reported the absolute photopeak efficiencies derived from simulations.

$\epsilon(\cdot 10^{-3})$	@P1	@P2	@P3	@P4	@P5
276keV	31.8 ± 0.9	4.5 ± 0.4	1.1 ± 0.2	/	/
302keV	27 ± 3	3.4 ± 0.2	1.1 ± 0.1	/	/
356keV	24.1 ± 0.5	2.73 ± 0.08	1.02 ± 0.08	/	/
383keV	22 ± 3	1.7 ± 0.2	0.9 ± 0.1	/	/
511keV	12.5 ± 0.1	1.24 ± 0.04	0.534 ± 0.009	0.204 ± 0.005	0.061 ± 0.003
661keV	11.44 ± 0.06	1.22 ± 0.02	0.41 ± 0.01	0.123 ± 0.006	0.030 ± 0.004
1173keV	5.14 ± 0.04	0.57 ± 0.01	0.189 ± 0.008	/	/
1274keV	4.52 ± 0.03	0.50 ± 0.01	0.174 ± 0.006	0.052 ± 0.004	0.023 ± 0.006
1332keV	4.43 ± 0.03	0.48 ± 0.01	0.162 ± 0.006	/	/

Table 9: Simulated absolute peak efficiency. The various position (P1, P2, P3,...) refers to those described in paragraph 2.1

5.3 Data analysis

Below, in the tables provided, you can find the various values of the %ID/g parameter measured, along with the corresponding histograms.

To facilitate the visualization and comparison of mice within the same category, histograms were grouped by mouse type and by the time interval between radiopharmaceutical administration and PET imaging.

28/11/2022 - CCK2R				
	30 minutes		2 hours	
	T1	T4	T0	T3
Brain	0.25 ± 0.03	0.33 ± 0.05	0.20 ± 0.03	0.09 ± 0.01
Heart	2.6 ± 0.8	1.7 ± 0.5	0.48 ± 0.06	0.7 ± 0.2
Liver	3.1 ± 0.3	2.9 ± 0.2	4.9 ± 0.4	3.3 ± 0.3
Spleen	1.5 ± 0.4	0.8 ± 0.2	0.57 ± 0.09	0.7 ± 0.2
Muscle	0.8 ± 0.2	0.4 ± 0.1	0.4 ± 0.1	0.22 ± 0.07
Bone	0.7 ± 0.2	0.09 ± 0.03	0.15 ± 0.05	0.12 ± 0.04
Pancreas	2.3 ± 0.7	2.7 ± 0.8	1.1 ± 0.3	0.7 ± 0.1
Lungs	3.8 ± 0.6	3 ± 1	3 ± 1	1.6 ± 0.5
Kidneys	4.7 ± 0.5	6.6 ± 0.8	4.3 ± 0.4	3.8 ± 0.5
Blood	4 ± 1	2.6 ± 0.8	2.5 ± 0.8	1.5 ± 0.4
Stomach	1.9 ± 0.3	13 ± 4	2.5 ± 0.7	1.1 ± 0.1
Tumor	11.8 ± 0.8	0.44 ± 0.04	38 ± 3	1.6 ± 0.1

Table 10: Parameters %ID/g measured on 28/11/2022

29/11/2022 - WT				
	30 minutes		2 hours	
	T2	T4	T1	T3
Brain	0.30 ± 0.04	0.30 ± 0.04	0.35 ± 0.06	0.037 ± 0.006
Heart	3.1 ± 0.6	1.7 ± 0.5	2.9 ± 0.9	0.31 ± 0.05
Liver	4.9 ± 0.4	4.1 ± 0.3	7.6 ± 0.6	2.6 ± 0.2
Spleen	0.75 ± 0.09	1.4 ± 0.3	1.1 ± 0.2	0.40 ± 0.08
Muscle	0.9 ± 0.3	1.2 ± 0.2	2.1 ± 0.6	0.30 ± 0.09
Bone	0.7 ± 0.1	0.5 ± 0.1	0.17 ± 0.05	0.022 ± 0.007
Pancreas	5 ± 1	2.8 ± 0.6	1.7 ± 0.5	0.8 ± 0.2
Lungs	7 ± 2	2.0 ± 0.3	4 ± 1	0.7 ± 0.1
Kidneys	11 ± 1	5.9 ± 0.5	7.8 ± 0.6	4.6 ± 0.8
Blood	1.5 ± 0.2	1.3 ± 0.2	0.7 ± 0.1	0.27 ± 0.04
Stomach	1.2 ± 0.1	0.89 ± 0.08	7 ± 1	0.46 ± 0.08
Tumor	5 ± 2	3.0 ± 0.9	1.7 ± 0.4	0.8 ± 0.2

Table 11: Parameters %ID/g measured on 29/11/2022

	13/12/2022 - WT			
	30 minutes		2 hours	
	T2	T4	T1	T3
Brain	0.25 ± 0.03	0.21 ± 0.04	0.12 ± 0.03	0.07 ± 0.02
Heart	3 ± 1	1.3 ± 0.4	0.8 ± 0.2	0.15 ± 0.05
Liver	3.6 ± 0.3	2.1 ± 0.1	3.8 ± 0.3	0.81 ± 0.07
Spleen	0.8 ± 0.2	0.8 ± 0.2	0.8 ± 0.2	0.11 ± 0.03
Muscle	0.9 ± 0.3	1.0 ± 0.3	0.24 ± 0.08	0.09 ± 0.03
Bone	0.033 ± 0.005	0.19 ± 0.02	0.039 ± 0.008	0.10 ± 0.02
Pancreas	2.3 ± 0.7	1.3 ± 0.4	1.2 ± 0.4	0.16 ± 0.06
Lungs	4 ± 1	1.0 ± 0.2	2.1 ± 0.6	0.26 ± 0.05
Kidneys	5.2 ± 0.4	4.0 ± 0.3	8 ± 1	1.2 ± 0.1
Blood	0.7 ± 0.1	0.53 ± 0.07	0.12 ± 0.03	0.32 ± 0.05
Stomach	3.6 ± 0.6	1.0 ± 0.2	0.41 ± 0.05	0.11 ± 0.02
Tumor	1.1 ± 0.3	0.18 ± 0.04	0.4 ± 0.1	0.10 ± 0.04

Table 12: Parameters %ID/g measured on 13/12/2022

	14/2/2023 - CCK2R					
	T7	T8	T9	T10	T11	T12
Brain	0.22 ± 0.06	0.27 ± 0.08	0.24 ± 0.07	0.17 ± 0.05	0.6 ± 0.2	0.18 ± 0.06
Heart	2.1 ± 0.7	3 ± 1	3 ± 1	2.5 ± 0.9	\	2.6 ± 0.9
Liver	4 ± 2	6 ± 2	4 ± 1	5 ± 1	3 ± 1	5 ± 2
Intestine	2.6 ± 0.7	0.9 ± 0.3	4 ± 2	4 ± 1	4 ± 1	10 ± 4
Spleen	3 ± 1	1.9 ± 0.7	1.8 ± 0.6	2.0 ± 0.7	4 ± 2	7 ± 2
Muscle	0.8 ± 0.3	1.4 ± 0.5	0.9 ± 0.3	1.1 ± 0.4	0.9 ± 0.3	1.9 ± 0.7
Bone	0.8 ± 0.3	1.7 ± 0.6	0.3 ± 0.1	0.09 ± 0.03	0.15 ± 0.04	0.007 ± 0.003
Pancreas	3 ± 1	3 ± 1	8 ± 4	2.1 ± 0.6	13 ± 5	7 ± 2
Lungs	2.8 ± 0.8	7 ± 3	4 ± 2	4 ± 1	2.9 ± 0.8	5 ± 2
Kidneys	6 ± 2	7 ± 2	4 ± 1	5 ± 2	4 ± 1	7 ± 2
Blood	4 ± 2	7 ± 3	6 ± 3	6 ± 3	4 ± 2	4 ± 1
Tumor	3.0 ± 0.8	0.6 ± 0.2	4 ± 2	4 ± 1	0.4 ± 0.1	1.6 ± 0.4

Table 13: Parameters %ID/g measured on 14/02/2023

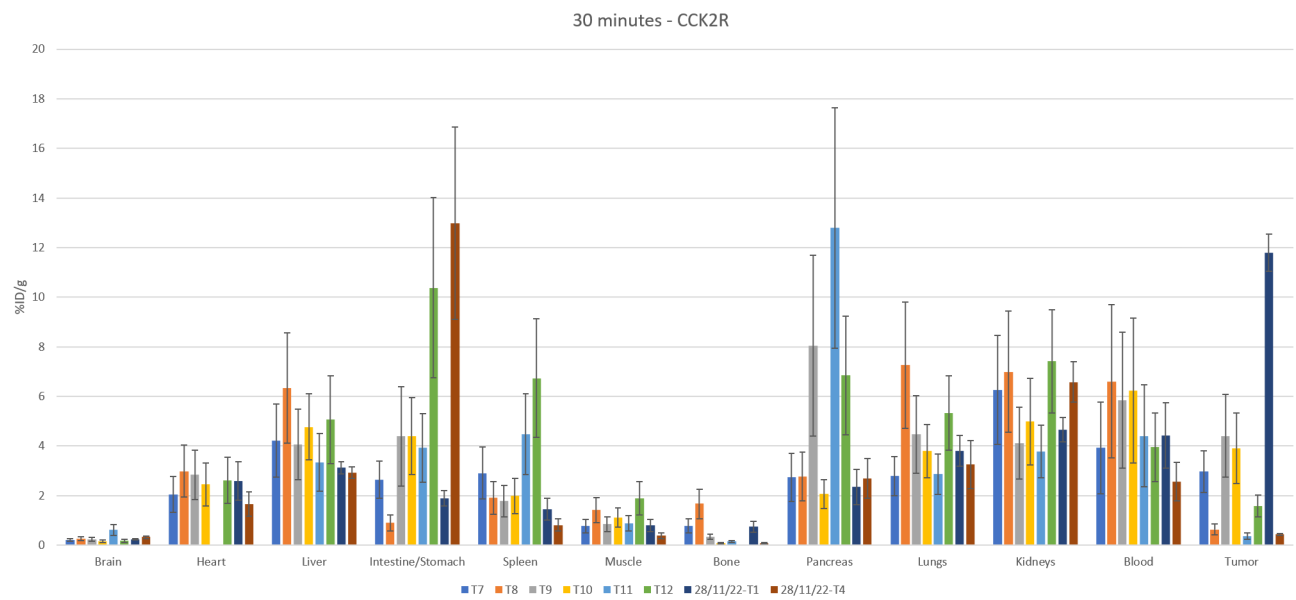


Figure 14: %ID/g for CCK2R mice, PET at 30 minutes

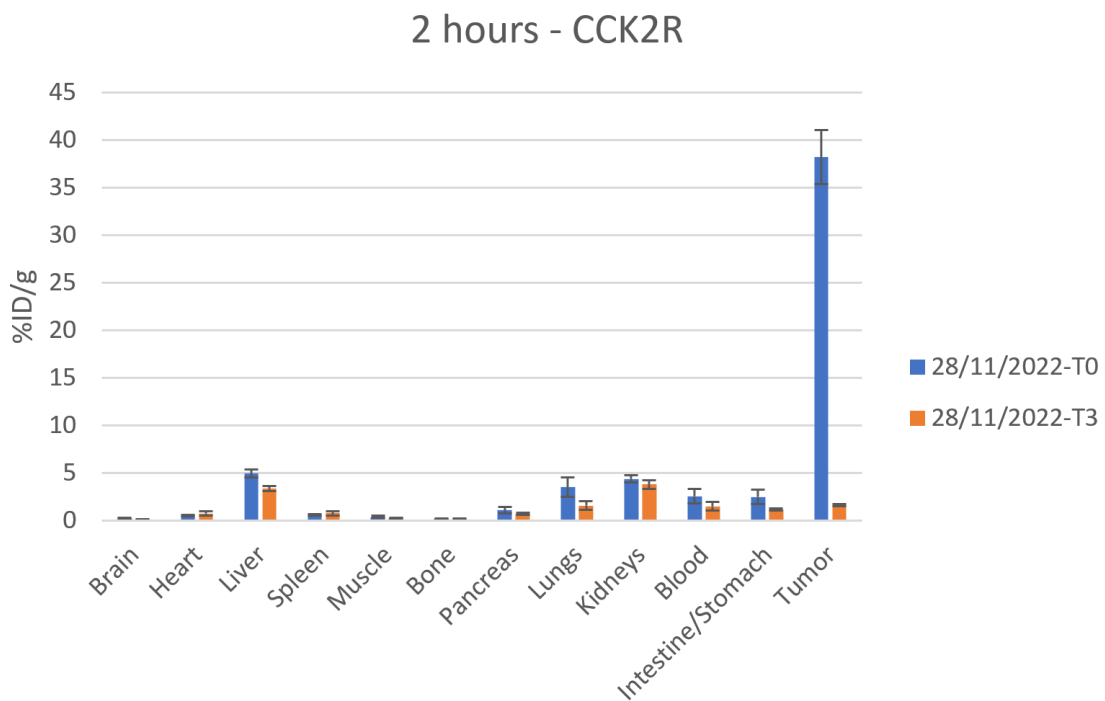


Figure 15: %ID/g for CCK2R mice, PET at 2 hours

30 minutes - WT

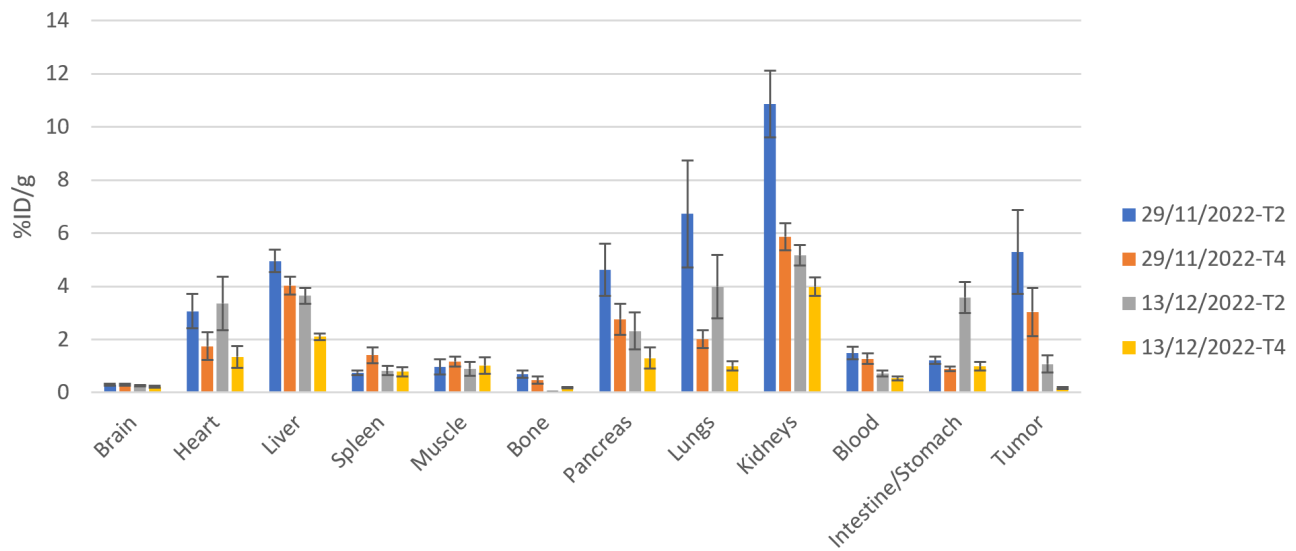


Figure 16: %ID/g for WT mice, PET at 30 minutes

2 hours - WT

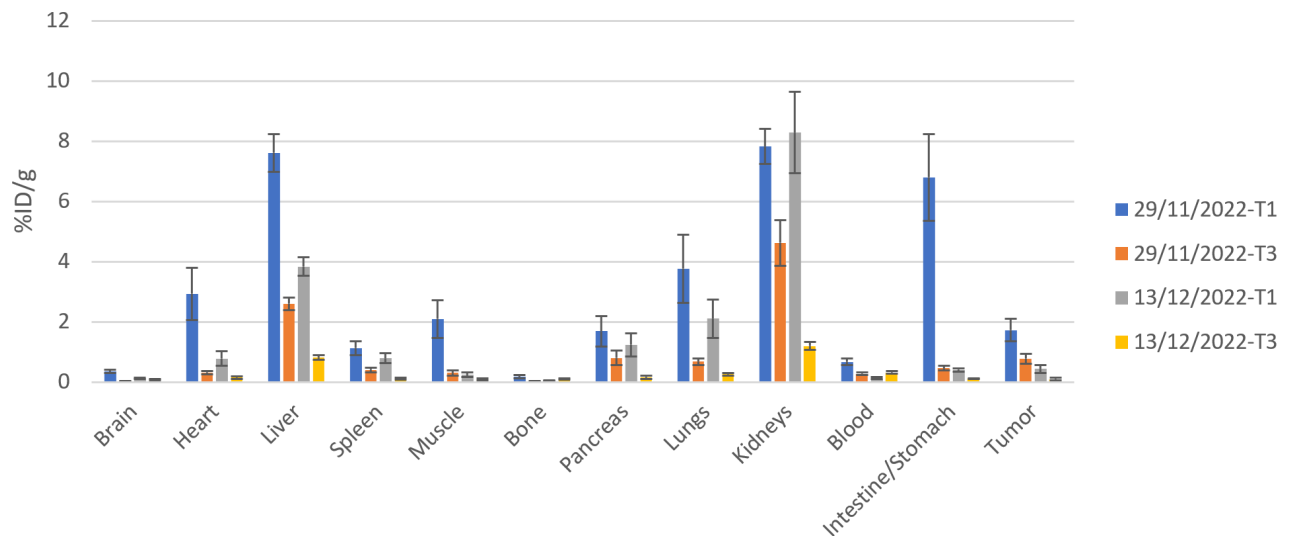


Figure 17: %ID/g for WT mice, PET at 2 hours

References

- [1] S. Liu (2008), "Bifunctional coupling agents for radiolabeling of biomolecules and target-specific delivery of metallic radioisotopes". *Adv Drug Deliv Rev* 60(12):1347-1370
- [2] A. Andriggetto (2022), "Production of radioisotopes for medicine". Trieste next, Talk's presentation
- [3] A. Andriggetto et al. (2019), "The ISOLPHARM project: ISOL-based production of radionuclides for medical applications". *Journal of Radioanalytical and Nuclear Chemistry* 322:73-77
- [4] L. Morselli (2023), "Production and Characterization of ^{111}Ag for radiopharmaceutical applications in the framework of the ISOLPHARM project", Ph.D. Thesis, Università degli Studi di Ferrara
- [5] L. Morselli (2021), "The ISOLPHARM collaboration: a facility for the production and study of innovative radiopharmaceuticals", Poster session, Euroschool on exotic beams